

Metrological characterization of consumer-grade equipment for wearable brain-computer interfaces and extended reality

*Original*

Metrological characterization of consumer-grade equipment for wearable brain-computer interfaces and extended reality / Arpaia, P; Callegaro, L; Cultrera, A; Esposito, A; Ortolano, M. - In: IEEE TRANSACTIONS ON INSTRUMENTATION AND MEASUREMENT. - ISSN 0018-9456. - STAMPA. - 71:(2022), p. 4002209. [10.1109/TIM.2021.3127650]

*Availability:*

This version is available at: 11583/2971065 since: 2022-09-07T13:41:00Z

*Publisher:*

IEEE-INST ELECTRICAL ELECTRONICS ENGINEERS INC

*Published*

DOI:10.1109/TIM.2021.3127650

*Terms of use:*

This article is made available under terms and conditions as specified in the corresponding bibliographic description in the repository

*Publisher copyright*

IEEE postprint/Author's Accepted Manuscript

©2022 IEEE. Personal use of this material is permitted. Permission from IEEE must be obtained for all other uses, in any current or future media, including reprinting/republishing this material for advertising or promotional purposes, creating new collecting works, for resale or lists, or reuse of any copyrighted component of this work in other works.

(Article begins on next page)

# Metrological characterization of consumer-grade equipment for wearable brain-computer interfaces and extended reality

Pasquale Arpaia<sup>1,2,3,\*</sup>, Luca Callegaro<sup>4</sup>, Alessandro Cultrera<sup>4</sup>, Antonio Esposito<sup>5,2</sup>, Massimo Ortolano<sup>5,4</sup>

**Abstract**—This paper proposes the characterization of stimulation and detection equipment in the design of wearable brain-computer interfaces based on visually evoked potentials. In particular, methods for the characterization of the optical output of commercial smart glasses, and for the calibration of a low-cost electroencephalograph are presented and discussed. The reported results show that, by proper characterization and calibration, consumer-grade equipment is suitable for brain-computer interface applications. Moreover, unexpected harmonics of the visual stimuli have to be taken into account by suitable processing. Finally, the electroencephalograph shows an adequate linear behavior, but its gain error of around 10% should be corrected by calibration in some applications.

**Index Terms**—brain-computer interface; extended reality; electroencephalography; calibration; characterization.

## I. INTRODUCTION

Brain-computer interfaces (BCI) are recently attracting much interest from the scientific and technological community [1]. Through a BCI, a novel mean of communication is provided by relying on direct measurement of brain signals. Applications have been addressed to either impaired and able-bodied people. Examples are robots control [2], industrial inspection [3], and neurorehabilitation [4], [5]. Among possible paradigms, reactive BCIs are the most performing ones [6], [7]. In a reactive paradigm, sensory stimulation is needed to elicit specific brain potentials. Therefore, when the BCI user is exposed to a stimulus, the correspondingly evoked potential can be detected. Recent studies have proven that visually evoked potential (VEP) are particularly suited for communication and control applications [3], [8], [9]. As a matter of fact, many BCIs are still limited to laboratory setups because, in uncontrolled conditions, artifacts compromise brain activity measurements [10]. However, many efforts have been made to bring BCI technology in daily life by focusing on wearable, portable, and low-cost devices [11]–[14].

The majority of works in the BCI field consider the electroencephalography to measure the electrical activity of neurons populations. In doing so, non-invasive systems can be implemented since electrodes can be placed outside the scalp [15]. Furthermore, the electroencephalography fits the

need for wearability, portability, and low cost. In these regards, some studies evaluated the usability of commercially-available headsets and compared consumer-grade electroencephalograph (EEG) with medical-grade one [16], [17]. It emerged that consumer-grade instrumentation can be employed in BCI applications, but clinical setups offer better data quality and reliability although more expensive. Notably, the cited studies validated the devices during experiments with human subjects, but they did not characterize the devices alone.

In line with the previous considerations, the elicitation of steady-state VEPs (SSVEP) is here taken into account. The discussion copes with the possibility to provide visual stimuli by means of smart glasses, which are increasingly exploited in virtual reality and augmented reality (i.e. extended reality, or XR) [18], and to detect the elicited potentials by means of a commercial EEG. In the BCI field, the user can interact with the XR glasses by merely staring at icons appearing on the display. Upon this simple principle, a user-friendly, low-cost, and performant BCI can be built by integrating smart glasses and EEG available off-the-shelf [3], [5], [9]. Previous researches already proved the functionality of wearable XR-BCI systems. However, the measured EEG signals occasionally show an unexplained behavior. In details, when a human subjects is stimulated with a flickering light, the harmonic content of the measured electroencephalogram does not match the one associated with the ideal stimulus. Literature studies suggest that the unexpected behaviors should be exclusively led back to the non-linearity of human brains [19]. In addition, it is well-known that brain signals are characterized by low signal-to-noise ratio and non-stationarity, which could affect their spectral distribution. Hence, various filtering techniques have been proposed in literature, e.g. empirical mode decomposition [20], [21] or multivariate empirical mode decomposition [22], [23]. Nevertheless, those studies were more application-oriented and they did not deal with a metrological characterization of the stimulation and detection equipment.

Commercially available smart glasses exploit different display technologies. In particular, optical see-through technology exploits semi-transparent displays that do not hide the real scene while superimposing virtual objects to it. Therefore, they are more suited for extended reality [18]. Typical devices exploit an LCD display with an active matrix of polysilicon thin-film-transistor, or silicon-based OLED matrix, or even planar waveguides showing different images to create a stereoscopic illusion. Currently, the calibration of smart glasses mostly concerns the accurate measurement of the user's eyes position [24] or display calibration for properly rendering of virtual objects [25]. Indeed, generating flickering icons with smart glasses is a recent proposal, and it is closely related to the BCI framework. Even in SSVEP-BCI research, previous works

<sup>1</sup>Department of Electrical Engineering and Information Technology (DI-ETI), Università degli Studi di Napoli Federico II, Naples, Italy.

<sup>2</sup>Augmented Reality for Health Monitoring Laboratory (ARHeMLab), Università degli Studi di Napoli Federico II, Naples, Italy

<sup>3</sup>Centro Interdipartimentale di Ricerca in Management Sanitario e Innovazione in Sanità (CIRMIS), Università degli Studi di Napoli Federico II, Naples, Italy

<sup>4</sup>INRIM - Istituto Nazionale di Ricerca Metrologica, strada delle Cacce 91, Turin, Italy.

<sup>5</sup>Department of Electronics and Telecommunications (DET), Politecnico di Torino, Corso Duca degli Abruzzi 24, Turin, Italy.

\*corresponding author: pasquale.arpaia@unina.it

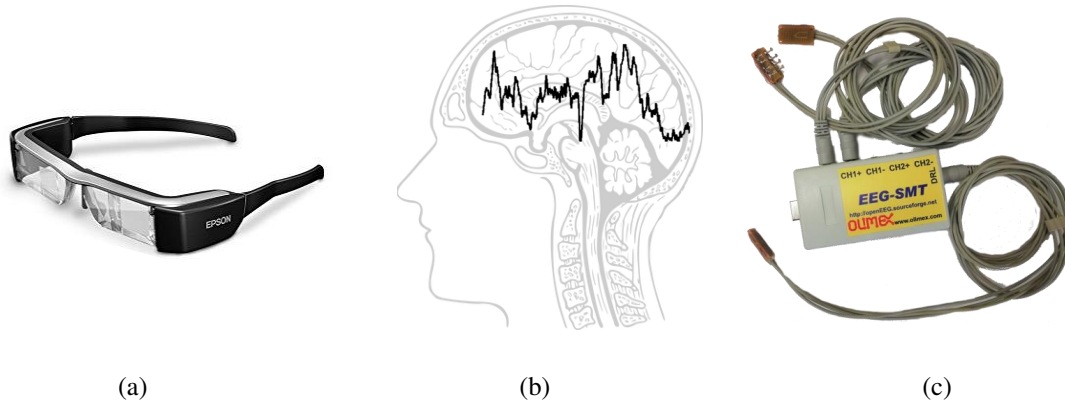


Figure 1: Wearable brain-computer interface based on steady-state visually evoked potentials: (a) smart glasses for visual stimulation, (b) the human user, (c) low-cost EEG.

dealt with the optimization of the stimulus layout [26] and the comparison of different implementation is usually application-oriented. Therefore, neither the properties of a flickering icon nor the EEG measurement accuracy have been assessed yet. The application-oriented approach did not allow to separate the different sources of errors and uncertainties, since neurophysiological phenomena are not yet fully understood [19]. For instance, in addition to the possible EEG measurement errors and uncertainties, there is no guarantee that smart glasses can generate visual stimuli responding to design specifications. In such a framework, the IEEE Standards Association has indicated a roadmap for neurotechnologies by considering standardized calibration procedures in addition to validation based on user tasks [27].

The present work aimed to characterize the stimulation and detection equipment of a wearable SSVEP-BCI, especially focusing on the generation of flickering icons with smart glasses and the calibration of an off-the-shelf EEG. This extends the preliminary results presented in [28], in which a preliminary characterization of the EEG was carried out. Such a characterization appears essential in the design of novel wearable interfaces. Therefore, in the remainder of the paper, the proposed characterization is presented in Section II. Next, results are presented and discussed in Section III. Conclusions follow in Section IV.

## II. CHARACTERIZATION OF STIMULATION AND DETECTION EQUIPMENT FOR SSVEP-BCI

The characterization of equipment for a BCI integrated with extended reality is here proposed with respect to a possible implementation. Notably, the Epson Moverio BT-200 and the Olimex EEG-SMT electroencephalograph are considered as representative devices for implementing such a system. These are building blocks of the typical wearable system represented in Fig. 1. In there, (i) smart glasses are used for generating flickering icons, (ii) the user transduces the visual stimulation into an electrical signal, and (iii) the EEG device measures the electrical brain activity. Relevant details about the two devices are reported in the following subsections. Then, methods for stimulus characterization and EEG calibration are presented.

### A. BT-200 smart glasses

The implementation discussed here includes the generation of a flickering icon with an Epson Moverio BT-200. These smart glasses feature an LCD display based on polysilicon thin-film-transistor active matrix with a refresh rate equal to 60 Hz. The size of each display is 0.42 inches with  $960 \times 540$  pixels resolution. Square white icons were implemented in Android with a dedicated graphic library [29]. With a simple approach, the flickering is obtained by switching pixels on and off at fractions of the refresh rate, in order to generate a square-wave stimulus. Rise and fall time associated with thin-film-transistor technology equal 10 ns to 100 ns. Therefore, the underlying technology should not limit the stimuli dynamics.

### B. EEG-SMT electroencephalograph

The detection stage of the SSVEP-BCI is an Olimex EEG-SMT [30]. This EEG consists of an acquisition board with two differential channels (each provided of two active dry electrodes and one reference electrode). The active electrodes contain an operational amplifier-based buffer for the rejection of high frequency interference and electrical decoupling. The schematic of the acquisition board [30] reports several stages for band-pass filtering and amplification. The bandwidth of the EEG is roughly 60 Hz with an adjustable gain in the range  $10^3 - 10^4$  (the device is designed for input voltages in the  $\mu\text{V}$  range). The acquired signal is digitized with a 10-bit ADC, and the full-scale range is 4 V. Sampled data are sent through a USB port to a PC.

### C. Characterization of the BT-200 optical output

The flickering icon generated by BT-200 was characterized in terms of harmonic content up to 100 Hz since this is usually the bandwidth of interest for the SSVEP stimulation [31]. Flickering frequencies nominally equal to 10 Hz and 12 Hz were primarily investigated because these were considered in recent SSVEP applications [13]. The BT-200 were programmed to display a single white square icon at the center of the lens. The icon's area was about 80% of the display area. For characterizing the flickering icon, a photo-transducer was

used and data were sent to a PC through USB. A picture of the setup is shown in Fig. 2. This setup included a photodiode soldered on a matrix board, a battery, and a board with a microcontroller.

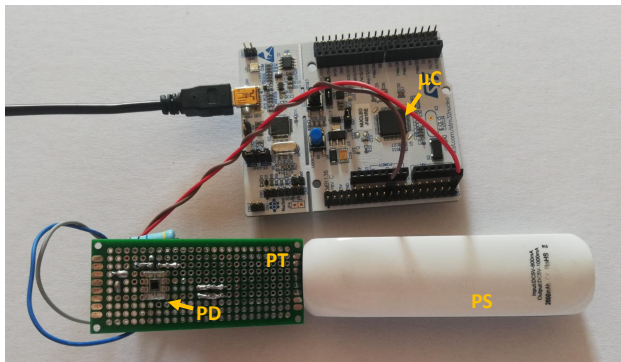


Figure 2: Photodiode-based transducer realized on a matrix board and connected to a microcontroller for signal acquisition (PS: power supply, PD: photodiode, PT: photo-transducer,  $\mu\text{C}$ : microcontroller).

The optical measurement system is schematically shown in Fig. 3, while the figure's labels are defined in Tab. I. The photo-transducer PT consists of a commercial photodiode PD integrated with a transimpedance amplifier (TIA) [32]. The photodiode circuit was powered by a power supply battery PS to avoid the line noise introduced by AC adapters. Inside PD, the photon-induced current is converted into voltage according to the feedback impedance. The output voltage is thus proportional to the optical output of the BT-200. An external resistor  $R_{\text{ext}}$  was connected to the TIA for achieving an optimal gain-bandwidth setting, namely  $11 \text{ V}/\mu\text{A}$  DC gain and  $1.3 \text{ kHz}$  bandwidth. Specifically, a microcontroller  $\mu\text{C}$  was exploited for measuring the output voltage and the gain value was set to match the full-scale range of the its ADC, equal to  $3.3 \text{ V}$ . The photo-transducer voltage was sampled at  $1 \text{ kHz}$ <sup>1</sup> with a 12-bit resolution. The sampled voltage  $V_{\text{BT}}$  was finally transmitted to the PC.

PT was placed in front of the BT-200 display. Its position was empirically determined by looking for the maximum measured voltage, so that the sensor was uniformly illuminated by the large icon. Measurements were carried out in a dark room to avoid that the ambient light could affect the results. Notably, the spectrum measured in absence of flickering had negligible amplitude. The output of PT was processed via MATLAB. Each acquisition lasted  $t_{\text{meas}} = 10 \text{ s}$ . The 10 s-long records were centered by subtracting the mean and then they were analysed in the frequency domain. Hanning windowing was applied before executing a fast Fourier transform (FFT) algorithm, thus reducing spectral leakage without greatly affecting harmonic amplitudes. From the FFT results, only the amplitude spectra

<sup>1</sup>The bandwidth of the ADC implies a Nyquist frequency of  $500 \text{ Hz}$ . Ideal square waves would introduce aliasing due to the  $75^{\text{th}}$  harmonic with an amplitude of about  $1\%$  of the fundamental harmonic in the range of  $100 \text{ Hz}$  (SSVEP frequency range of interest). However, measurements performed during the PT design showed negligible contribution from harmonics of that order and above. Therefore, no anti-aliasing filter was implemented to keep the circuit configuration as simple as possible.

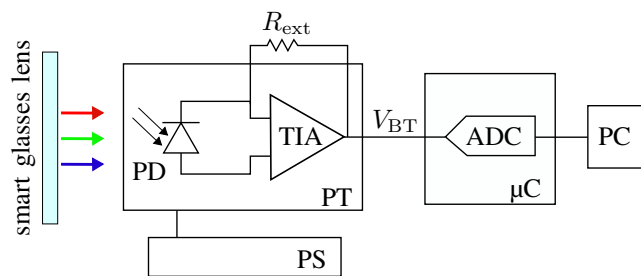


Figure 3: Schematic diagram of the setup for characterizing the BT-200 optical output.

were derived. Then, each spectrum was normalized with respect to the amplitude of the first harmonic. Amplitude spectra were normalized to the first harmonic, for purpose of comparison between different sets of measurements. The measures of  $V_{\text{BT}}$  were also analysed in time domain.

#### D. Calibration of the EEG-SMT

The EEG was characterized at frequencies in the  $1 \text{ Hz}$  to  $100 \text{ Hz}$  range, in accordance with characterization of the BT-200 optical output. Both the linearity and the magnitude error were assessed. Then, non-stationarity of the EEG was evaluated as well by checking for long-term drifts over several months. The measurement setup was implemented with laboratory instrumentation and commercially available components, and it can be easily reproduced in most electrical engineering laboratories without exploiting specialized EEG test units. The basic idea was to generate a large voltage signal with high accuracy and then scale it down to the measurement range of interest ( $\mu\text{V}$ ). In doing so, accuracy and traceability are much greater than directly generating a small calibration signal [28], [33]. Instead, when using EEG test units available on the market, specific calibration might be required in order to ensure accuracy and traceability.

The coaxial schematic of the calibration setup is shown in Fig. 4, while the figure's labels are defined in Tab. II. The signal  $V_S$  is generated by means of the channel Ch A of SG and the unity-gain amplifier AMP, which guarantees electrical decoupling while driving the current for the following stages. The signal  $V_S$  is digitized with the calibrated voltmeter V. At the same time, the calibration signal  $V_{\text{CAL}}$  is obtained by scaling down  $V_S$  through two cascaded voltage divider stages. The first stage, IVD, is inductive and provides a scaling factor  $k_{\text{IVD}}$ . The second stage, RVD, is resistive and provides a scaling factor  $k_{\text{RVD}}$ . The calibration signal  $V_{\text{CAL}}$  appears between Ch 1+ and Ch 1- of the EEG. The "drive right leg" (DRL) input, which reduces common mode voltage through a feedback loop, is connected to the signal ground. In each acquisition,  $V_{\text{CAL}}$  is sampled for an amount of time  $t_{\text{meas}} = 16 \text{ s}$ .

The large-amplitude sinusoidal signal  $V_S$  was generated with the DAC of SG using 1000 samples per period, with a peak amplitude of  $\sqrt{2} \text{ V}$  of frequency  $f$  in the range  $1 \text{ Hz}$  to  $100 \text{ Hz}$ , though frequencies up to the  $\text{kHz}$  range could

Table I: Labels and instrumentation employed in the setup of Fig. 3

Symbol	Instrument	Model
PD	Photodiode	Texas Instruments OPT101, monolithic photodiode and single-supply transimpedance amplifier
$R_{\text{ext}}$	10 M $\Omega$ resistor	carbon composition resistor with 1 % tolerance
PS	Battery	power bank with 5 V-1000 mA DC output and 2600 mA h electric charge
$\mu\text{C}$	Microcontroller	STMicroelectronics STM32F401RE embedded on a Nucleo64 board for general purpose applications

Table II: Labels and instrumentation employed in the setup of Fig. 4

Symbol	Instrument	Model
SG	Generator	National Instruments PCI-6733, 10 V range, 16 bit resolution
AMP	Amplifier	Unity-gain custom buffer amplifier with differential input based on INA 111 opamp
V	Voltmeter	Keysight 3458A multimeter, DCV digitizing mode
IVD	Inductive voltage divider	Electro Scientific Instruments PRT-73, 7-decade automatic precision ratio transformer, 2.5 V Hz <sup>-1</sup> option
RVD	Resistive ratio divider	Composed of $R_1$ and $R_2$
$R_1$	100 k $\Omega$ resistor	New Resistance A02 series resistor with BPO MUSA connectors
$R_2$	10 $\Omega$ resistor	Vishay H series resistors with BPO MUSA connectors

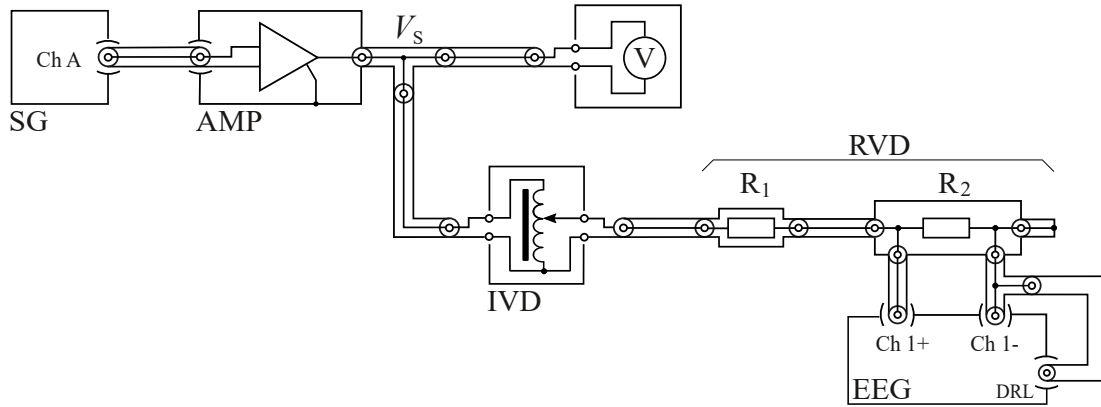


Figure 4: Coaxial schematic diagram of the EEG calibration setup.

be investigated as well with the proposed setup [33]. The voltmeter V was used for the coherent sampling of  $V_S$  in the measurement full scale of 1 V, with 5000 samples per measurement. The IVD was used with ratio  $k_{\text{IVD}}$  in the range 0.1 to 1.0 during the experiments. For the implementation of RVD, thick film resistors were used. Their nominal values were  $R_1 = 100 \text{ k}\Omega$  and  $R_2 = 10 \Omega$ , respectively, thus resulting in  $k_{\text{RVD}} = 10^{-4}$ . These settings allowed for the generation of a calibration signal  $V_{\text{CAL}}$  with an rms value in the range  $10 \mu\text{V}$  to  $100 \mu\text{V}$ . The EEG sample frequency was set at 256 Hz and operated to digitize  $V_{\text{CAL}}$ . The data acquired from this single differential channel were collected and stored in the PC to be processed via MATLAB.

In order to assess the linearity and the magnitude error of the EEG, both the digitized signals  $V_S$  and  $V_{\text{EEG}}$  were fitted by using a four-parameter sinefit algorithm [34], implemented in MATLAB according to the IEEE standard [35]. The fitting returned amplitude  $A$  and offset  $O$  of  $V_S$  and  $V_{\text{EEG}}$ . The rms value of the signals of interest was calculated as

$$V_{\text{rms}} = \sqrt{\frac{A^2}{2} + O^2}, \quad (1)$$

obtaining  $V_{S,\text{rms}}$  and  $V_{\text{EEG},\text{rms}}$ . The rms value of the calibration signal  $V_{\text{CAL}}$  was calculated from  $V_{S,\text{rms}}$  as

$$V_{\text{CAL},\text{rms}} = k_{\text{IVD}} k_{\text{RVD}} V_{S,\text{rms}}. \quad (2)$$

The accuracy of  $V_{\text{CAL}}$  (and its rms value) can be assessed from the accuracy of the individual components of (2). By applying the law of propagation of uncertainties, it results

$$\frac{u(V_{\text{CAL},\text{rms}})}{V_{\text{CAL},\text{rms}}} = \sqrt{\left[\frac{u(k_{\text{RVD}})}{k_{\text{RVD}}}\right]^2 + \left[\frac{u(k_{\text{IVD}})}{k_{\text{IVD}}}\right]^2 + \left[\frac{u(V_{S,\text{rms}})}{V_{S,\text{rms}}}\right]^2}, \quad (3)$$

where the relative uncertainties of each term from (2) appear. Concerning RVD, the resistors  $R_1$  and  $R_2$  are respectively measured as two-terminal and four-terminal standards in DC, with a calibrated precision multimeter. The uncertainty of the factor  $k_{\text{RVD}}$  was thus quantified as  $u(k_{\text{RVD}}) = 13 \times 10^{-6}$ . Next, the uncertainty of  $k_{\text{IVD}}$  was quantified as  $u(k_{\text{IVD}}) = 30 \times 10^{-6}$  based on the inductive divider specifications and factory calibration certificate. Finally, the uncertainty associated with  $V_S$  was quantified as  $u(V_{S,\text{rms}}) = 64 \times 10^{-6}$ . For a discussion on the origin of these contributions see Section 3 in [33].

Preliminary estimates from components and tolerance values given in the EEG schematic [30] provided a rough estimate of the  $V_{\text{EEG}}$  tolerance of about 10%. Given these considerations,  $V_{\text{CAL},\text{rms}}$  can be considered highly accurate.

Henceforth, in order to calibrate the EEG in the frequency range of interest, the error  $\epsilon$  of the EEG relative to  $V_{\text{CAL},\text{rms}}$  was defined as follows

$$\epsilon = \frac{V_{\text{EEG},\text{rms}} - V_{\text{CAL},\text{rms}}}{V_{\text{CAL},\text{rms}}}. \quad (4)$$

### III. RESULTS AND DISCUSSION

In this section, results are reported for both the BT-200 characterization and the EEG calibration. By assessing errors and uncertainties in utilising such equipment, the operation of wearable SSVEP-BCIs can be better understood.

#### A. Flickering icons spectra

As a representative result of the behaviour of the BT-200, Fig. 5 reports the measured spectrum of a 12 Hz flickering icon nominally generated as a square-wave with 50% duty cycle. Harmonics amplitudes are plotted in relative terms with respect to the first harmonic. Recall that, as a figure of merit, an ideal square wave is characterized by a 50% duty cycle and a spectrum with only odd harmonics weighted by  $1/n$ , where  $n$  is the harmonic order (with  $n = 1, 3, 5, \dots$ ). Evidently, the BT-200 device did not produce a flickering signal with the expected shape. For instance, even harmonics are also present and harmonic ratios are not consistent with the ones of a square wave. In addition, the inset of Fig. 5 shows that the signal in the time domain appears smoother than a square wave and that its duty cycle does not equal 50%.

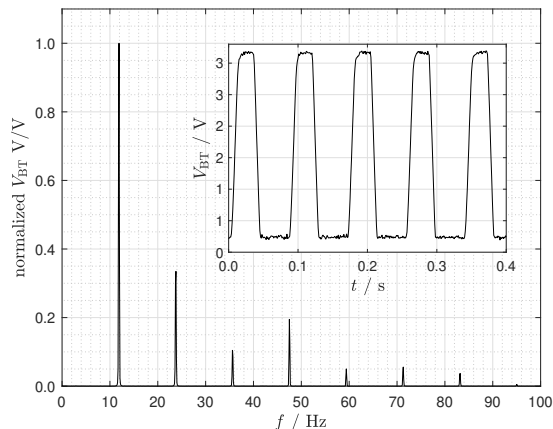


Figure 5: Measured spectrum of an icon generated by the BT-200 flickering at 12 Hz (inset:  $V_{BT}$  in time domain).

The smoothing of the signal can be explained by two facts. First, the flickering is limited by the display refresh rate equal to 60 Hz. Hence, the wave has a 40% duty cycle, which is associated with the presence of even harmonics. Second, independently of the duty cycle, the waveform appears smoothed with an asymmetric profile, which again produces even harmonics. It must be stressed that the asymmetric profile of the waveform edges suggests that the signal is indeed distorted and a low-pass filtering of the measurement setup can be excluded.

Flickering frequencies associated with an even number of frames were also tested. In those cases, a 50% duty cycle could be achieved. Indeed, measurement results for 10 Hz flickering still showed even harmonics, though much attenuated with respect to the ones of Fig. 5. In time domain, the curve still appeared smoothed with respect to an ideal square wave, but the duty cycle is close to 50%. However,

the flickering signal does not have a square-wave shape yet. In order to compare the measurement results associated with the 10 Hz and the 12 Hz flickering, Tab. III reports the harmonic ratio for the 3<sup>rd</sup> and 5<sup>th</sup> harmonics and the measured duty cycle. For the sake of clarity, the harmonic ratios and duty cycle of the nominal square wave are reported as well. Please note that the measured harmonic ratios are approximated so that they can be reported as  $1/n$  where  $n$  is an integer.

These results suggest different scenarios for using smart glasses in BCI. Operationally, the detection of SSVEP relies upon extracting either odd or even harmonics [3], [9], thus the non-idealities of the stimuli do not pose particular issues. Meanwhile, the spectral content of the light source must be handled when aiming to study the brain response to visual stimuli [19], [31]. For instance, a 12 Hz-like icon cannot be a square wave by design, while amplitude accuracy would be not even guaranteed in 10 Hz-like cases. Therefore, characterizing the optical output of smart glasses appears essential in such applications.

	nominal	10 Hz	12 Hz
3 <sup>rd</sup> harmonic	1/3	1/3	1/10
5 <sup>th</sup> harmonic	1/5	1/7	1/20
duty cycle	50%	51%	39%

Table III: Comparison between the nominal square wave harmonic ratios and duty cycle and the measured flickering signals at 10 Hz and 12 Hz.

#### B. EEG linearity and magnitude error

As a preliminary analysis, the digitized  $V_S$  is compared to  $V_{EEG}$  to show that the signal  $V_{CAL}$  is suitable for the EEG calibration. In particular, the amplitude spectrum of the large-amplitude signal  $V_S$  and  $V_{EEG}$ , at frequency  $f = 20$  Hz, are reported in Fig. 6. Hanning windowing was applied before the FFT algorithm. Both spectra were normalized to the amplitude of the first harmonic. It can be seen that the signal-to-noise ratio of  $V_S$ , and as a consequence with  $V_{CAL}$ , is much higher than the signal-to-noise ratio of  $V_{EEG}$ . This justifies the suitability of employing the generated voltage in calibrating the EEG. Note that Fig. 6 shows some higher order harmonic content for both  $V_S$  and  $V_{EEG}$ , and this will contribute to the type A uncertainty of the calibration points. The spectrum of the EEG also shows a 50 Hz reasonably coming from the PC connection.

Thereafter, the EEG linearity was investigated. Measurements were conducted by varying the amplitude of  $V_{CAL}$  through setting  $k_{IVD}$ . Results are shown in Fig. 7, where  $V_{EEG,rms}$  is plotted as a function of  $V_{CAL,rms}$  for  $f = 20$  Hz. A linear behavior is clearly visible. Moreover, the comparison between the slope of the interpolated line with the nominal response (unitary gain and zero offset) points out gain and offset errors. In details, applying linear regression resulted in a slope  $\beta_1 = 1.095$  and a non-zero intercept  $\beta_0 = -0.079$ . Then, the following results concerning the magnitude error also reveal that the line slope does change with frequency. The goodness of fitting for this linear regression was also tested.

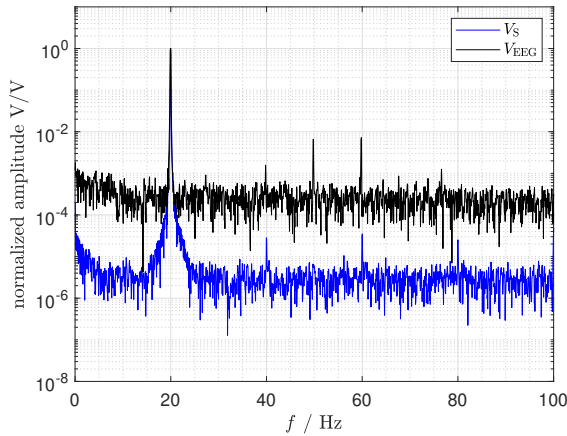


Figure 6: Amplitude spectrum of  $V_S$  and  $V_{EEG}$  at 20 Hz in logarithmic scale (normalized amplitudes).

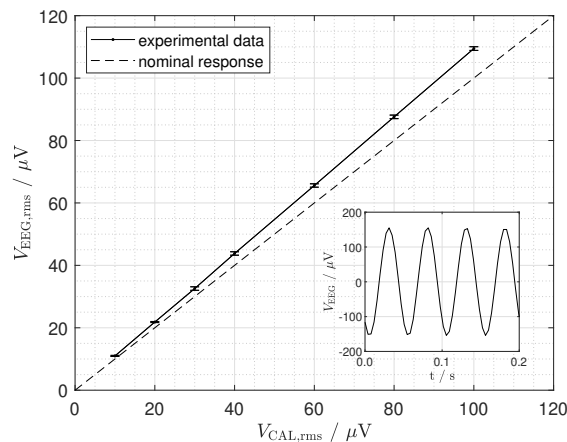


Figure 7: Root mean square (rms) values of  $V_{EEG}$  as a function of the rms of  $V_{CAL}$  for measuring linearity at 20 Hz (inset:  $V_{EEG}$  in time domain at  $V_{CAL,rms} = 100 \mu V$ ).

The linearity of the EEG was assessed again after several months (eight) to highlight eventual drift of the EEG under test. While confirming the linear behavior, the slope was increased to  $\beta'_1 = 1.105$  in the first measures set, and then it dropped to  $\beta''_1 = 1.099$  in a second set of measures. This suggested that there was no long-term drift, but a further uncertainty contribution had to be taken into account for the gain. Such uncertainty was quantified by considering the standard deviation of the measured slopes and in relative terms it resulted  $u_{B,lin} = 0.9\%$ . Since drifts of the EEG devices were excluded, possible non-stationarity in the measured signals should be exclusively attributed to brain activity.

The gain error  $\epsilon$  of the EEG relative to the calibration signal was calculated according to (4) by setting  $V_{CAL,rms} = 100 \mu V$ . The gain error curve is reported in Fig. 8. The  $\epsilon$  varies between  $-15\%$  and  $10\%$ . At  $f = 20$  Hz, the relative gain error is  $\epsilon \approx 10\%$ , in accordance with the linearity analysis result. By interpolating the calibration points with their uncertainty, the cut-off frequency at  $-3$  dB  $f_H$  was evaluated to be in the 54.5 Hz to 57.1 Hz range, which is reasonably close to the

nominal value of 59 Hz [30]. Meanwhile, at low frequencies, the gain error decreases in accordance with the high-pass filtering, whose cut-off frequency is nominally equal to  $f_L = 0.1$  Hz. It is worth mentioning that the IVD could attenuate  $V_{CAL}$  because of loading effects of its cores at frequency  $f < 10$  Hz. Indeed, measurements performed with a lock-in amplifier connected in place of the EEG showed some effect only below  $f = 1$  Hz, with an attenuation of  $V_{CAL,rms}$  of about 1%. Nonetheless, at this frequency, the attenuation due to the EEG band-pass filter is much larger.

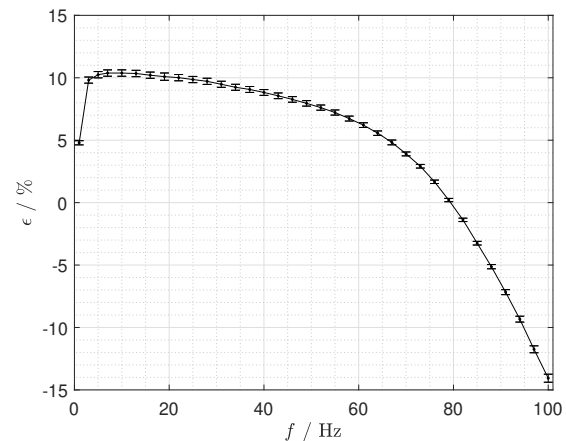


Figure 8: Calibration curve representing the relative difference  $\epsilon$  between  $V_{DUT,rms}$  and  $V_{CAL,rms}$ .

Fig. 8 also reports the extended uncertainty of the calibration point with a coverage factor  $k = 4$ . The extended uncertainties of the calibration points were obtained by propagating the uncertainty of  $V_{EEG,rms}$  and  $V_{CAL,rms}$  to the  $\epsilon$  defined in eq. (4). In type A uncertainty evaluation, the uncertainty associated with sinefit parameters was taken into account. According to [36], the uncertainty associated with  $A$  and  $O$  can be derived by the residual errors of the sinefit, which allow to calculate the variance of the parameters estimators. Meanwhile, in type B uncertainty evaluation, the contribution arising from repeated linearity measurements was taken into account for  $V_{EEG,rms}$ , while the tolerances of  $k_{IVD}$  and  $k_{RVD}$  as well as the voltmeter reading accuracy were considered for  $V_{CAL,rms}$ . As a result, the largest absolute uncertainty on  $\epsilon$  is  $\pm 0.32\%$  and it is associated with  $f = 100$  Hz. These last results can be generalized to different values of  $V_{CAL,rms}$  thanks to the previously assessed linear behaviour.

As a final step, simulations were performed with the Monte Carlo method by replicating the EEG schematic [30] in LTSpice. In there, components values and their declared tolerance were exploited. Fig. 9 reports the result of these simulations in comparison with the experimental gain error curve. The different gray levels are related to the probability of assuming such values. Three ranges are here represented: the inner 50% range (from 25<sup>th</sup> to 75<sup>th</sup> percentile) in dark gray, the inner 90% range (from 5<sup>th</sup> to 95<sup>th</sup> percentile) in gray, and the range of all possible values (between extremes) in light gray. Note that the measured response of the EEG is substantially explained by the components tolerance. In

particular, the main component to the discrepancy between the simulated and measured response could be led back to the difference between the nominal and actual value of a trimmer used for adjusting the EEG overall gain [30].

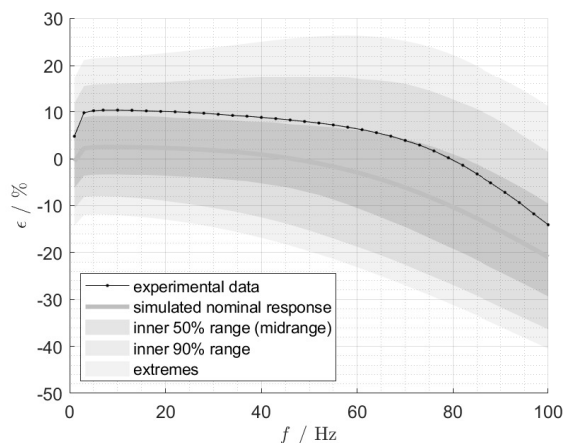


Figure 9: Comparison between the measured gain error of Fig. 8 (black line with bars) and the simulated gain error (gray). The gray shaded areas represent the distribution of possible values due to components tolerances. For the sake of clarity, error bars of experimental data have been omitted.

Given the strong linear behavior and smooth gain error obtained with the characterization of this EEG, which can reasonably be considered representative for a class of consumer-grade equipment, the results suggest that the detection part of recent SSVEP-BCI [3], [9] can be straightforwardly implemented. Nonetheless, from the metrological point of view, when utmost accuracy and traceability to the international system of units are needed, the proposed method is suitable for the EEG calibration.

### C. On-field test of SSVEP-BCI

Results of the characterization presented above can be used to draw some consideration about real-situation SSVEP-BCI applications and are here briefly discussed considering on-field measurements with a human subject (following the scheme shown in Fig. 1). Fig. 10 compares i) electroencephalographic data measured from the subject stimulated with an icon flickering at 12 Hz for 120 s (red curve) with ii) the  $V_{BT}$  stimulus measurement of Fig. 5 (black curve). Both of them are normalized to the first harmonic in order to focus on harmonic ratios. Indeed, SSVEP classification algorithms are based on harmonics detection without typically caring of absolute amplitude values. Meanwhile, absolute amplitude could be interesting in characterizing the human brain response, but proper experiments should be designed to control associated uncertainty sources. EEG data are corrected with the values of  $\epsilon$  taken from the calibration points of Fig. 8. Error bars were calculated as the combined uncertainty of the EEG measurements (type-A) and the uncertainty of calibration points (type-A and type-B). The uncertainty of  $\epsilon$  (in the order of 0.4 %) is substantially smaller than the one of the EEG measurements

(in the order of 14 %) in the whole EEG bandwidth (60 Hz). It can be noted that the EEG spectrum presents a sharp harmonic distribution, featuring all the harmonics already present in the visual stimulus  $V_{BT}$  within the EEG bandwidth. On the other hand, the amplitudes of the peaks in the EEG data do not correspond, and neither are compatible within the error at the corresponding peaks amplitudes in  $V_{BT}$ . Considered that given the characterization in section III-B the non-linearity of the EEG is negligible, and other instrumental effects on this EEG in on-field SSVEP-BCI applications were excluded by earlier results [3], it can be reasonably ruled out that the EEG could have altered the subject-generated EEG signals enough to produce such a discrepancy. Nevertheless, this observation seem to be in compliance with previous literature [19], [31], where the discrepancy between the harmonic content of the visual stimulus and the one of the EEG spectra could be led back to non-linearity introduced by the human subject.

In summary, given the results of section III and these on-field measurements, it is reasonable to expect that in SSVEP-BCI application distinguish-ability of the harmonic components can be quite easily assessed even with consumer-grade equipment. On the other hand, any insight on the amplitude response of the subject to the harmonic components must rely on a careful characterization of the optical output of the stimulation equipment.

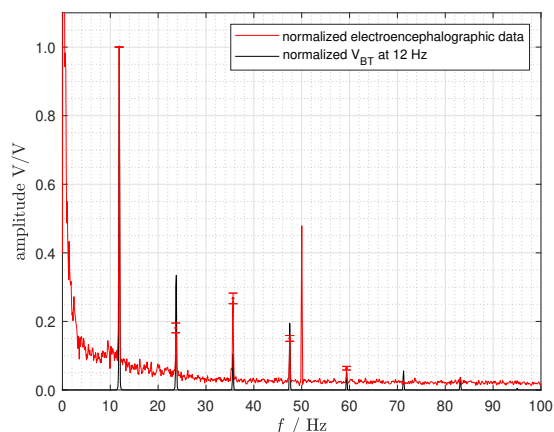


Figure 10: Electroencephalographic data acquired with the calibrated EEG in correspondence to a 12 Hz flickering icon generated with the BT-200. Spectra are normalized in order to be compared.

## IV. CONCLUSIONS

In this paper, consumer-grade equipment for wearable SSVEP-BCI has been tested. The optical output generated by flickering an icon with commercial smart glasses, produced well-separated harmonics, but also unwanted harmonics that can be a limitation for some applications. Hence the choice of the visual stimulation technology may strongly depend on the particular purpose. Concerning the acquisition of electroencephalographic signals, the tested EEG showed strong linearity and a gain error that was quantified. Moreover, no long-term drift was observed. The outcome of the calibration suggests



that this component of the BCI chain would not pose particular limitations to the majority of SSVEP-BCI applications. On-field test of the equipment corroborated these considerations.

As a final remark, a quantitative approach to the characterization of consumer-grade equipment for BCI applications would substantially integrate the more common user task validation procedures found in literature. Such an approach is in agreement with the needs expressed by the roadmap for neurotechnologies that was recently proposed by the IEEE Standards Association.

#### ACKNOWLEDGEMENTS

This work was carried out as part of the "ICT for Health" project, which was financially supported by the Italian Ministry of Education, University and Research (MIUR), under the initiative 'Departments of Excellence' (Italian Budget Law no. 232/2016), through an excellence grant awarded to the Department of Information Technology and Electrical Engineering of the University of Naples Federico II, Naples, Italy.

#### REFERENCES

- [1] S. Saha, K. A. Mamun, K. I. U. Ahmed, R. Mostafa, G. R. Naik, S. Darvishi, A. H. Khandoker, and M. Baumert, "Progress in Brain Computer Interface: Challenges and Potentials," *Frontiers in Systems Neuroscience*, vol. 15, p. 4, 2021.
- [2] L. Bi, X.-A. Fan, and Y. Liu, "EEG-based brain-controlled mobile robots: a survey," *IEEE transactions on human-machine systems*, vol. 43, no. 2, pp. 161–176, 2013.
- [3] L. Angrisani, P. Arpaia, A. Esposito, and N. Moccaldi, "A Wearable Brain-Computer Interface Instrument for Augmented Reality-Based Inspection in Industry 4.0," *IEEE Transactions on Instrumentation and Measurement*, vol. 69, no. 4, pp. 1530–1539, 2019.
- [4] S. R. Soekadar, N. Birbaumer, M. W. Slutzky, and L. G. Cohen, "Brain-machine interfaces in neurorehabilitation of stroke," *Neurobiology of disease*, vol. 83, pp. 172–179, 2015.
- [5] P. Arpaia, L. Duraccio, N. Moccaldi, and S. Rossi, "Wearable brain-computer interface instrumentation for robot-based rehabilitation by augmented reality," *IEEE Transactions on Instrumentation and Measurement*, vol. 69, no. 9, pp. 6362–6371, 2020.
- [6] X. Xing, Y. Wang, W. Pei, X. Guo, Z. Liu, F. Wang, G. Ming, H. Zhao, Q. Gui, and H. Chen, "A high-speed SSVEP-based BCI using dry EEG electrodes," *Scientific reports*, vol. 8, no. 1, pp. 1–10, 2018.
- [7] H. Wang, Z. Pei, L. Xu, T. Xu, A. Bezerianos, Y. Sun, and J. Li, "Performance Enhancement of P300 Detection by Multiscale-CNN," *IEEE Transactions on Instrumentation and Measurement*, vol. 70, pp. 1–12, 2021.
- [8] T.-H. Nguyen and W.-Y. Chung, "A single-channel SSVEP-based BCI speller using deep learning," *IEEE Access*, vol. 7, pp. 1752–1763, 2018.
- [9] M. Wang, R. Li, R. Zhang, G. Li, and D. Zhang, "A wearable SSVEP-based BCI system for quadcopter control using head-mounted device," *IEEE Access*, vol. 6, pp. 26789–26798, 2018.
- [10] J. Minguillon, M. A. Lopez-Gordo, and F. Pelayo, "Trends in EEG-BCI for daily-life: Requirements for artifact removal," *Biomedical Signal Processing and Control*, vol. 31, pp. 407–418, 2017.
- [11] L.-D. Liao, S.-L. Wu, C.-H. Liou, S.-W. Lu, S.-A. Chen, S.-F. Chen, L.-W. Ko, and C.-T. Lin, "A novel 16-channel wireless system for electroencephalography measurements with dry spring-loaded sensors," *IEEE Transactions on Instrumentation and Measurement*, vol. 63, no. 6, pp. 1545–1555, 2014.
- [12] Y.-H. Yu, S.-W. Lu, C.-H. Chuang, J.-T. King, C.-L. Chang, S.-A. Chen, S.-F. Chen, and C.-T. Lin, "An inflatable and wearable wireless system for making 32-channel electroencephalogram measurements," *IEEE Transactions on Neural Systems and Rehabilitation Engineering*, vol. 24, no. 7, pp. 806–813, 2016.
- [13] L. Angrisani, P. Arpaia, D. Casinelli, and N. Moccaldi, "A single-channel SSVEP-based instrument with off-the-shelf components for trainingless brain-computer interfaces," *IEEE Transactions on Instrumentation and Measurement*, vol. 68, no. 10, pp. 3616–3625, 2018.
- [14] P. Arpaia, N. Moccaldi, R. Prevete, I. Sannino, and A. Tedesco, "A wearable eeg instrument for real-time frontal asymmetry monitoring in worker stress analysis," *IEEE Transactions on Instrumentation and Measurement*, vol. 69, no. 10, pp. 8335–8343, 2020.
- [15] R. Abiri, S. Borhani, E. W. Sellers, Y. Jiang, and X. Zhao, "A comprehensive review of eeg-based brain-computer interface paradigms," *Journal of neural engineering*, vol. 16, no. 1, p. 011001, 2019.
- [16] W. D. Hairston, K. W. Whitaker, A. J. Ries, J. M. Vettel, J. C. Bradford, S. E. Kerick, and K. McDowell, "Usability of four commercially-oriented EEG systems," *Journal of neural engineering*, vol. 11, no. 4, p. 046018, 2014.
- [17] E. Ratti, S. Waninger, C. Berka, G. Ruffini, and A. Verma, "Comparison of medical and consumer wireless EEG systems for use in clinical trials," *Frontiers in human neuroscience*, vol. 11, p. 398, 2017.
- [18] D. Chatzopoulos, C. Bermejo, Z. Huang, and P. Hui, "Mobile augmented reality survey: From where we are to where we go," *IEEE Access*, vol. 5, pp. 6917–6950, 2017.
- [19] M. Labecki, R. Kus, A. Brzozowska, T. Stacewicz, B. S. Bhattacharya, and P. Suffczynski, "Nonlinear origin of ssvep spectra—a combined experimental and modeling study," *Frontiers in computational neuroscience*, vol. 10, p. 129, 2016.
- [20] A. Given and T. Batbat, "Evaluation of filters over different stimulation models in evoked potentials," *Biocybernetics and Biomedical Engineering*, vol. 39, no. 2, pp. 339–349, 2019.
- [21] S. Duraivel, A. T. Rao, C. W. Lu, J. N. Bentley, W. C. Stacey, C. A. Chestek, and P. G. Patil, "Comparison of signal decomposition techniques for analysis of human cortical signals," *Journal of Neural Engineering*, vol. 17, no. 5, p. 056014, 2020.
- [22] N. Rehman and D. P. Mandic, "Multivariate empirical mode decomposition," *Proceedings of the Royal Society A: Mathematical, Physical and Engineering Sciences*, vol. 466, no. 2117, pp. 1291–1302, 2010.
- [23] N. Ur Rehman and D. P. Mandic, "Filter bank property of multivariate empirical mode decomposition," *IEEE transactions on signal processing*, vol. 59, no. 5, pp. 2421–2426, 2011.
- [24] J. Grubert, Y. Itoh, K. Moser, and J. E. Swan, "A survey of calibration methods for optical see-through head-mounted displays," *IEEE transactions on visualization and computer graphics*, vol. 24, no. 9, pp. 2649–2662, 2017.
- [25] M. Klemm, F. Seebacher, and H. Hoppe, "High accuracy pixel-wise spatial calibration of optical see-through glasses," *Computers & Graphics*, vol. 64, pp. 51–61, 2017.
- [26] X. Zhao, C. Liu, Z. Xu, L. Zhang, and R. Zhang, "Ssvep stimulus layout effect on accuracy of brain-computer interfaces in augmented reality glasses," *IEEE Access*, vol. 8, pp. 5990–5998, 2020.
- [27] IEEE Standards Association, "Neurotechnologies for Brain-Machine Interfacing." <https://standards.ieee.org/industry-connections/neurotechnologies-for-brain-machine-interfacing.html>.
- [28] P. Arpaia, L. Callegaro, A. Cultrera, A. Esposito, and M. Ortolano, "Metrological characterization of a low-cost electroencephalograph for wearable neural interfaces in industry 4.0 applications," in *2021 IV Workshop on Metrology for Industry 4.0 and IoT (MetroInd4.0&IoT)*, IEEE, 2021.
- [29] M. Segal and K. Akeley, "The OpenGL Graphics System: A Specification (Version 4.0, Core Profile)." <https://www.khronos.org/registry/OpenGL/specs/gl/glspec40.core.pdf>, 2010.
- [30] Olimex Ltd., "Schematics of the EEG-SMT device for electroencephalography." <https://www.olimex.com/Products/EEG/OpenEEG/EEG-SMT/resources/EEG-SMT-SCHEMATIC-REV-B.pdf>.
- [31] C. S. Herrmann, "Human eeg responses to 1–100 hz flicker: resonance phenomena in visual cortex and their potential correlation to cognitive phenomena," *Experimental brain research*, vol. 137, no. 3, pp. 346–353, 2001.
- [32] Texas Instruments, "OPT101 Monolithic Photodiode and Single-Supply Transimpedance Amplifier (Rev. B)." <https://www.ti.com/document-viewer/OPT101/datasheet/abstract#SBBS0022723>.
- [33] A. Cultrera, D. Corminboeuf, V. D'Elia, N. T. M. Tran, L. Callegaro, and M. Ortolano, "A new calibration setup for lock-in amplifiers in the low frequency range and its validation in a bilateral comparison," *Metrologia*, 2021.
- [34] IEEE Standards Association, "IEEE 1057-2017 - IEEE Standard for Digitizing Waveform Recorders." <https://standards.ieee.org/standard/1057-2017.html>.
- [35] Marko Neitola, "Four-Parameter Sinefit." <https://it.mathworks.com/matlabcentral/fileexchange/23214-four-parameter-sinefit>, 2021.
- [36] P. Händel, "Amplitude estimation using ieee-std-1057 three-parameter sine wave fit: Statistical distribution, bias and variance," *Measurement*, vol. 43, no. 6, pp. 766–770, 2010.